Dual-Polarized Wideband Low-Sidelobe Slot Array Antenna for V-Band Wireless Communications

Liu, Peiye; Pedersen, Gert Frølund; Hong, Wonbin; Zhang, Shuai

Published in:
I E E E Transactions on Antennas and Propagation

DOI (link to publication from Publisher):
10.1109/TAP.2023.3285086

Publication date:
2023

Document Version
Accepted author manuscript, peer reviewed version

Dual-Polarized Wideband Low Sidelobe Slot Array Antenna for V-Band Wireless Communications

Peiye Liu, Gert Frølund Pedersen, *Senior Member IEEE*, Wonbin Hong, *Senior Member IEEE*, Shuai Zhang, *Senior Member IEEE*

***Abstract*—A dual-polarized wideband low sidelobe slot array antenna for wireless communication systems in the V-band is proposed in this work. Taylor distribution is applied with each radiating slot as a tapering unit in both polarizations. A compact 2 × 2 elements subarray is designed to achieve stable amplitude and phase distribution among elements with two sets of integrated compact wideband unequal power dividers for the E- and H-planes inside the subarray. Then, two layers of orthogonally polarized feeding networks with unequal E-plane T-junction power dividers are used to connect the subarrays to two standard waveguides WR-15 as input ports. The prototype of 8 × 8 elements is fabricated and measured in an anechoic chamber. The maximum measured gain is 25.3 dBi and 25.4 dBi for V- and H-polarization, respectively. The overlapped impedance bandwidth is from 57 to 66.4 GHz with reflection coefficiencies below −10 dB, and the isolation between two input ports is around 35 dB. Sidelobe levels of both polarizations are below −22 dB with good agreement with the simulations.**

***Index Terms*—Dual-polarized, slot array antenna, low sidelobe, wideband, unequal power divider, Taylor distribution, V-band.**

I. Introduction

Planar array antennas were attracting more attention in academic and industrial areas and have been widely studied in recent years. With its low profile, small volume, and lightweight characteristics, the application has significant advantages in directive radio links. Compared to widely used reflector antennas with bulky structures, planar array antennas are simpler in manufacturing, assembling, and installation and less costly in packaging and delivery. Especially in the fifth-generation (5G) system and beyond, the rapidly increased demand for high capacity and transmit rates pushed the research towards a high-frequency range with wide absolute bandwidth [1], such as high-definition video streaming, high-speed internet, high-definition multimedia interface, and automotive radars. The V-band (57 - 66 GHz) with 9 GHz bandwidth, which is license-free and available almost worldwide, got more attention in such applications [2], [3].

Much effort has been put into the research to solve the challenges of planar array antennas. One is to achieve high gain and high antenna efficiency. Conventional printed circuit board (PCB) based antennas such as patch arrays with stripline or microstrip-line are no longer a good choice due to their high loss in the feeding network in the millimeter-wave frequency range. It significantly lowers the antenna gain as the array size increase in V-band. As presented in [4], although low-loss PCB Rogers RT/Duroid 6002 was used, the measured gain is still not entirely satisfactory. The research of substrate-integrated waveguide (SIW) and low-temperature co-fired ceramic (LTCC) based array antenna showed some improvement [5]–[7], but the dielectric loss could still lead to the peak gain drop to a large extent. On the contrary, the ohmic losses of the hollow waveguides (HW) are not significant at the millimeter-wave band. And the losses can be decreased by using materials with high electric conductivity and improving the surface roughness of the sample. However, the air gap between layers could cause power leakage. Some methods were introduced to enhance the metal contact, such as the diffusion bonding technic and gap waveguides [8]–[12]. However, the fabrication procedure becomes complicated, time-consuming, or costly. Metal 3D printing technic could realize the sample in one piece to avoid power leakage [13], [14]. However, the accuracy control can not meet the requirement up to V-band and higher. On the other hand, a hollow waveguide with an E-plane feed network is an alternative way to minimize the power leakage at the millimeter wave. It was first introduced in [15] and has been proven effective at E-band [16].

Another challenge that limits the application is the radiation pattern of the planar array antenna. To minimize the interferences from unexpected sources, sidelobe levels (SLL) are preferred to be as low as possible. As specified by the European telecommunications standards institute (ETSI) [17], several radiation-pattern-envelop standards set different maximum sidelobe level requirements. Most designs mentioned above are limited by their high SLL with uniform excitation among antenna elements. Besides the high gain challenge, most efforts were put into achieving low SLL characteristics in recent studies. A continuous transverse stub array proposed in [18] reaches low SLL patterns in the parallel plate waveguide (PPW) plane, but the structure is bulky and complicated in fabrication. In [19], [20], arrays are inclined by certain angles to avoid the array synthesis planes with the highest sidelobe level. However, SLLs are not suppressed in all other azimuth planes in these designs, as ETSI requires. Then the interference problem still exists. One effective method is to use the Taylor synthesis to design non-uniform excitation in the array elements [21]. As in [22], [23], array antennas based on E-plane hollow waveguide and inverted microstrip gap waveguide (IMGW) with Taylor synthesis achieved corresponding wideband and low SLL performance. However, 2 × 2 elements subarrays are excited as tapering units in the

This work was supported by the Modular Advanced Radio for Satellite Services (MARS2) project. (Corresponding author: Shuai Zhang).

Peiye Liu, Gert Frølund Pedersen, and Shuai Zhang are with the Antennas, Propagation and Millimeter-Wave Systems Section, Department of Electronic Systems, Aalborg University, 9220 Aalborg, Denmark (e-mail: sz@es.aau.dk).

Wonbin Hong is with the Department of Electrical Engineering, Pohang University of Science and Technology, Pohang 37673, South Korea (e-mail: whong@postech.ac.kr).

design, which leads to SLL rising between 30° to 50° away from the boresight. To suppress the SLL rising, a double-slit layer structure is introduced in [24]. It is only effective in the target plane SLL suppression, and the overall thickness of the prototype is increased. A low SLL antenna with multi-level compact unequal power dividers is introduced in [16]. Taylor synthesis is applied with each element as a tapering unit, which ensures a smooth SLL envelop of the radiation pattern. However, the structure is too complicated to be implemented in dual-polarization arrays. The significant advantage of dual-polarization antennas is the doubled system capacity, which is commonly preferred in wireless communications. A dual-circular-polarization low SLL Parallel-Plate Long-Slot (PPLS) array is reported in [25]. The maximum SLL achieved is −18.5 dB with unequal power dividers in the feeding network. But the bandwidth is relatively narrow. Another dual-polarization low SLL array design based on the gap waveguide has a similar issue [26]. The maximum SLL of −18.5 dB is achieved in a fractional bandwidth of only 5%.

In this study, a novel dual-polarized low SLL slots array antenna is proposed. The advantage of the structure is that it achieves low SLL performance in a wide bandwidth in the two polarizations. Also, amplitude tapering is adopted as each element is weighted as an independent unit. The sidelobe rising issue that cause is effectively avoided. The independent weighting in both polarizations is enabled by the proposed compact 2 × 2 elements subarray and the wideband unequal power dividers. These components can provide stable amplitude tapering and phase balance. An 8 × 8 element prototype working at V-band is fabricated and measured to validate the design.

The article is organized as follows. The overall array geometry and the array synthesis are illustrated in Section II. The operating mechanism of the compact 2 × 2 elements subarray is described in Section III. Then in Section IV, three types of unequal power dividers for subarrays and feeding networks are described and analyzed. In Section V, the entire feeding networks for the two polarizations and the final optimized results of the antenna are presented. The measured results of the prototype are presented and discussed in Section VI. Then, the conclusions are given in Section VII.

II. Antenna Geometry

Fig. 1 shows the geometry of the proposed 8 × 8 slots array antenna, which consists of five layers. The aperture size of the array is 32 mm × 32 mm. Cross-shaped slots are used as the radiating elements in the top layer for two polarizations. The 2 × 2 elements subarray works as a one to four power divider. The two layers below slots are the E- and H-plane unequal power dividers integrated inside subarrays. Orthogonal feeding network layers for the Vertical and Horizontal polarizations ensure power distributions among the subarrays. Then, they are fed by two standard waveguides (Wr-15) with transition sections from the bottom. All simulations in this work are done with the CST Microwave Studio (CST).

The element spacing is 4 mm which corresponds to 82 % wavelength of the center frequency. To avoid SLL rising

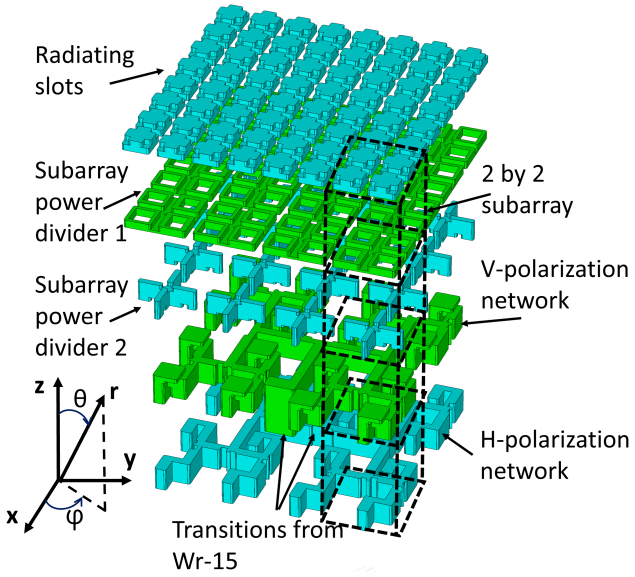

Fig. 1. Geometry of the proposed 8 × 8 slots antenna array with two-layer feeding networks.

between 30° to 50° [16], [24], Taylor distribution is applied as each slot as one tapering unit with the help of two-level unequal power dividers inside the subarrays and one in the feeding networks. The first SLL is chosen as −25 dB in the calculation for both polarizations. Taylor synthesis with $\widetilde{N} = 4$ is adopted. The calculated three power-split ratios are 1.3 dB, 3.37 dB, and 5.61 dB, respectively. The first two ratios are adopted inside subarrays, and the last one is in the T-junction in the feeding networks.

III. Design of the Subarray

The perspective view of the 2 × 2 elements subarray, the detailed view of the E-plane power divider layer, and the feeding layer one are shown in Fig. 2. Within the limited space of the subarray, E- and H-plane power dividers are adopted into two separate layers. The power-split ratios of the dividers can be adjusted separately for both planes and polarizations. Two layers of L-shaped waveguides are used as the feeding networks for the two polarizations. Feeding layer one is for V-polarization, and feeding layer two is for H-polarization. A small brick is inserted into the feeding layer one to ensure the isolation between the two ports [27]. An extra step is added to improve the impedance matching, as shown in Fig. 2(c). The subarray is optimized with two sets of periodic boundaries. Its material is brass (91 %) from the CST material library. The electric conductivity is 2.74×10^7 S/M, which is close to the properties of the material used in the fabrication. Moreover, the surface roughness is 0.0008 mm that can be controlled by the Computer numerical control (CNC) machine from the workshop.

The power-split ratios are set equal for all power dividers in the initial design to check the reflections and isolation performance of the subarray. The bricks in E- and H-plane power dividers have the same dimensions and positions. The subarray is biaxially symmetrical. The simulated E-field distributions for both polarizations at the center frequency in different layers are shown in Fig. 3, while ports one and two are excited

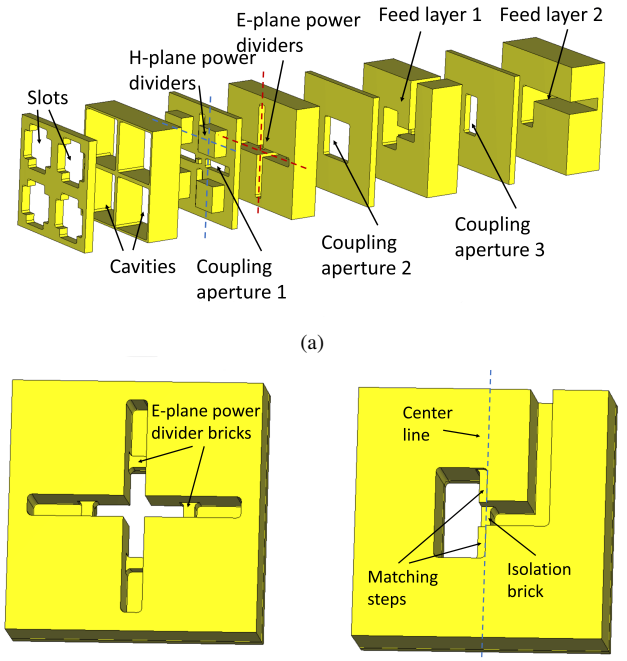

Fig. 2. The perspective view of (a) the 2 × 2 elements subarray, detailed view of (b) the E-plane power dividers, and (c) feeding network one.

Table I. Optimized dimensions of the subarray for the results in Fig. 4

	Width	Length	Height
Slot	2.16mm	3.38mm	0.7mm
Cavities	3.8mm	3.8mm	2.32mm
H-plane power divider bricks	2mm	2mm	1.08mm
Matching pin	0.34mm	0.34mm	0.3mm
Coupling aperture 1	0.72mm	2.97mm	0.5mm
E-plane power divider cavities	0.72mm	7.17mm	2.13mm
E-plane power divider bricks	0.38mm	0.72mm	0.76mm
Coupling aperture 2	3.04mm	3.04mm	0.54mm
Isolation brick	0.34mm	0.83mm	1.48mm
Matching step	0.3mm	3.04mm	0.35mm
Feeding network 1 branch A	0.83mm	2.12mm	2.8mm
Feeding network 1 branch B	0.75mm	3.8mm	2.8mm
Coupling aperture 3	1.44mm	3.04mm	0.5mm
Feeding network 2 branch A	1.44mm	3.04mm	2.7mm
Feeding network 2 branch B	0.97mm	4.28mm	2.7mm
Feeding network 2 branch A offset	0.72mm		

separately. The short branch A of the L-shape in feeding network 2 has an offset from the subarray centerline. It can be seen from Fig. 3(a) and 3(b) that when port one is excited, only weak power leaks into the feeding layer two. Moreover, when port two is excited, the power propagating into the feeding layer one is cut off by the narrow neck of branch A, which ensures good isolation between the two polarizations. E-field distributions in the above layers indicate a good polarization purity. The final optimized results are shown in Fig. 4. The

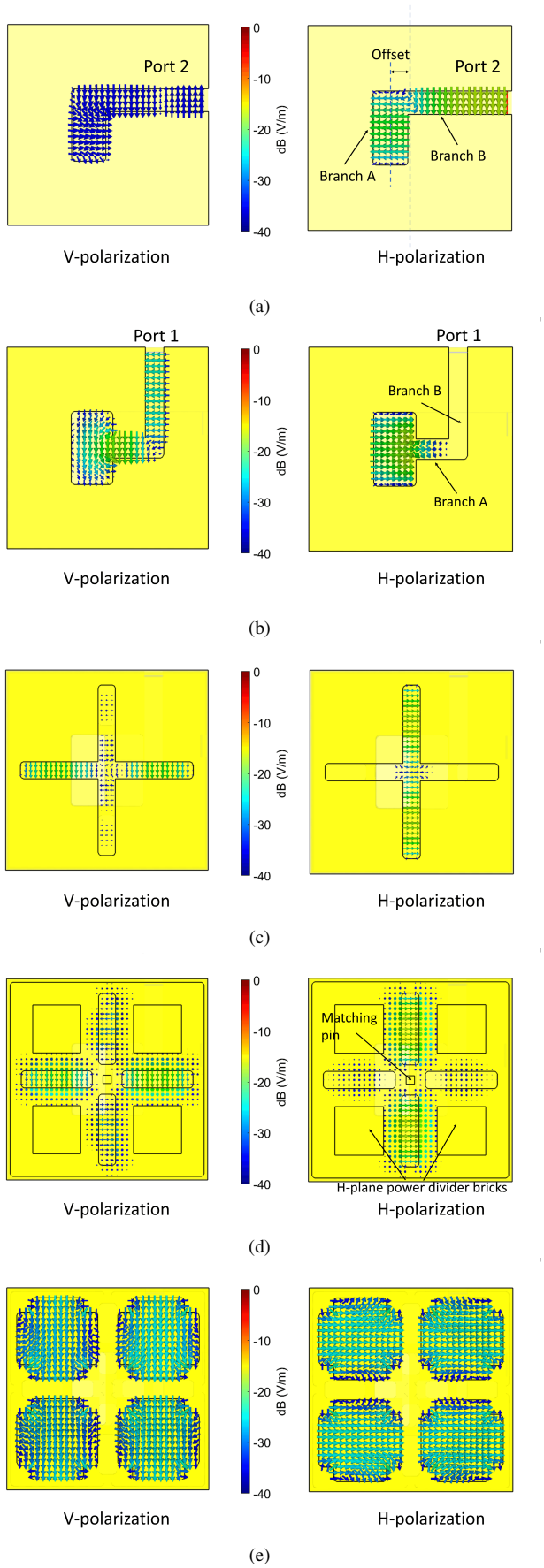

Fig. 3. E-fields distribution in (a) feeding layer 2, (b) feeding layer 1, (c) E-plane power dividers, (d) H-plane power dividers, and (e) slot layer.

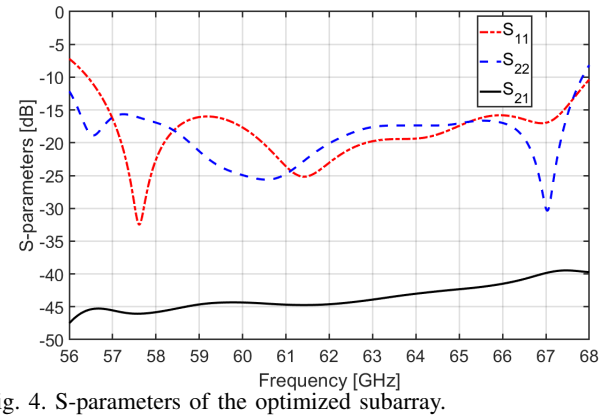

Fig. 4. S-parameters of the optimized subarray.

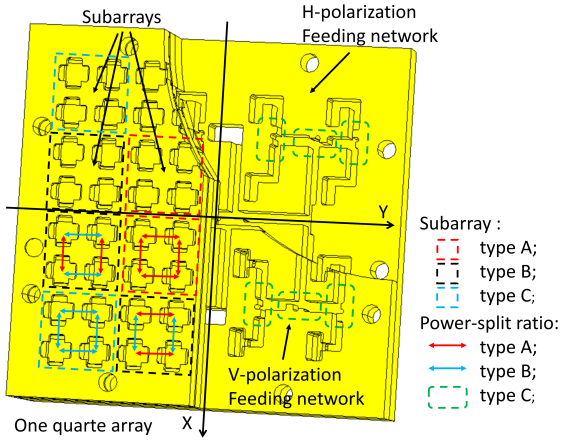

Fig. 5. Subarray and feeding network power dividers.

overlapped frequency range is from 57 to 67 GHz with the reflections of both ports below −15 dB. The isolation is around −40 dB. Optimized parameters are listed in Table I.

IV. Design of Unequal Power Dividers

Three different types of unequal power dividers are designed in this work, E- and H-plane subarray power dividers and T-junctions in feeding networks. As mentioned in Section II, three different power-split ratios are required to achieve low SLL performance of the 8 × 8 elements array. As shown in Fig. 5, ratios of type A (1.3 dB) and type B (3.37 dB) are required by E- and H-plane subarray power dividers to form the three different combinations of power distributions in sub-arrays. T-junction with a power-split ratio of type C (5.61 dB) is used to connect subarrays in both feeding networks.

A. E-plane Subarray Unequal Power Divider

Table II. Optimized dimensions and position of the bricks of the different types of E-plane power dividers.

E-plane power divider	Height	Width	Offset
Ratio Type A	0.42mm	0.5mm	0.44mm
Ratio Type B	1.14mm	0.5mm	0.49mm

The structure of the E-plane subarray unequal power divider is similar to the one proposed in [16]. In this work, the two

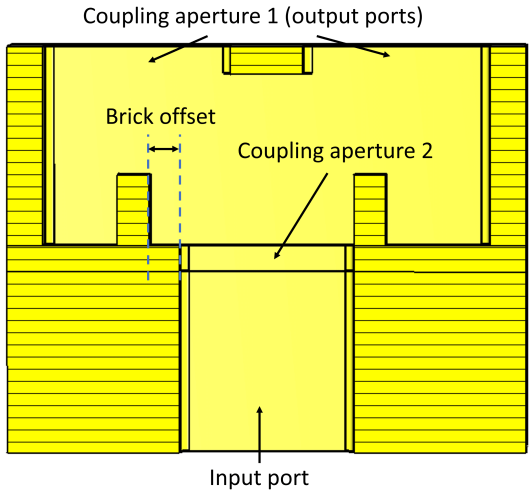

Fig. 6. Cross-secional view of the E-plane subarray unequal power divider.

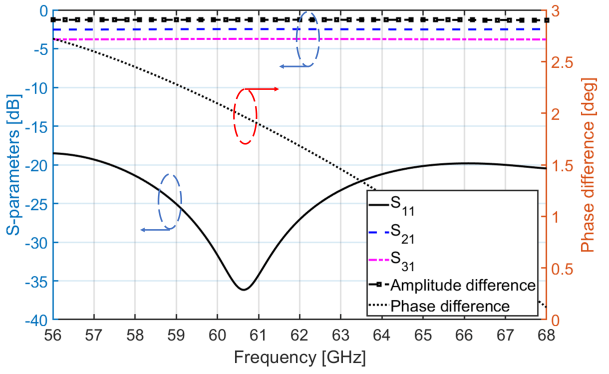

(a)

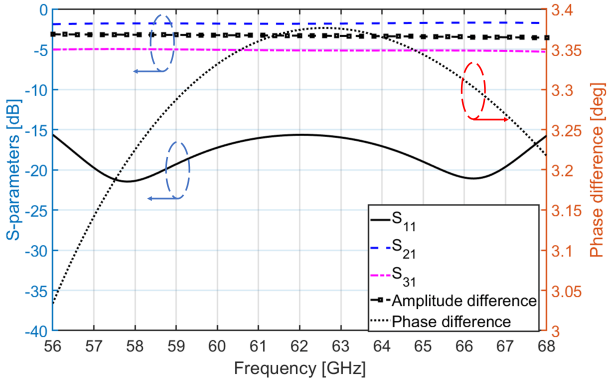

(b)

Fig. 7. Optimized S-parameters and phase difference over the frequency with power-split ratios of (a) type A 1.3 dB, (b) type B3.37 dB.

output branches are used as the feed of the H-plane unequal power dividers with the coupling aperture one instead of directly exciting the radiating slots. The cross-sectional view of the E-plane subarray power divider layer is shown in Fig. 6. The path difference is achieved by offsetting one of the bricks. Also, by changing the height of the bricks, the power-split ratio can be adjusted. The phase unbalances caused by path differences can be compensated by adjusting the width and

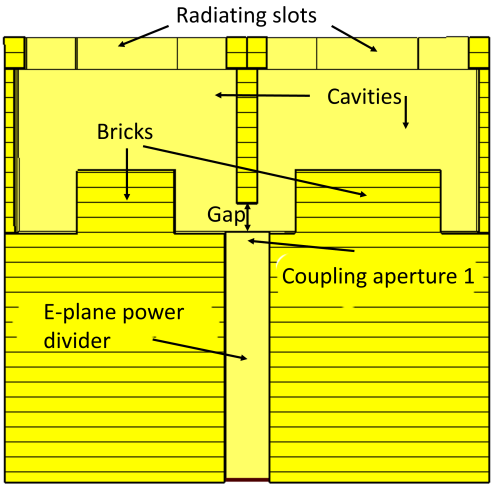

Fig. 8. Cross-secional view of the H-plane subarray unequal power divider.

offset distance of the bricks [16].

These three parameters are optimized to get the two power-split ratios, and the results are shown in Fig. 7. It can be seen that the reflection coefficients remain below −15 dB for both ratios. Moreover, the phase differences over the frequency are within 3.4°. The amplitude difference between the two output branches for power divider type A is -1.3 ± 0.1 dB. As the power-split ratio of type B increases, the amplitude variation over the frequency becomes large but is still within an acceptable range of -3.37 ± 0.15 dB. Dimensions and offset distance of the bricks are listed in Table II. The structure is simulated with two sets of perfect electric conductor (PEC) boundaries. The influences from the neighboring elements and structures above are not considered in the simulations. These values are further optimized in the full subarray simulations.

B. H-plane Subarray Unequal Power Divider

H-plane subarray unequal power dividers are cascaded on top of the E-plane subarray unequal power dividers to achieve Taylor distribution in the orthogonal planes. The same power split ratios of types A and B are required. The cross-sectional view of the H-plane subarray unequal power divider is shown in Fig. 8. Two dotted lines in the H-plane power divider layer in Fig. 2 indicate orthogonal cutting planes. Its working principle is similar to that of the E-plane power divider. In the design, the same dimensions of radiating slots and cavities are used. The bricks in cavities are of the same height. The power split ratio is controlled by the length difference of the bricks in the cutting plane, which could introduce different path characteristics. The bigger the length difference is, the larger the power split ratio is achieved. Then by changing the brick height, the phase balance between the two branches can be adjusted. The dimensions of the cavity, cross-slot, and gap size are optimized to get good S-parameters.

The optimized results of two types of H-plane power dividers are plotted in Fig. 9. The power split ratios are monitored using the 1-D field plot function in the field monitor of CST. The monitored planes are along the slot centerline

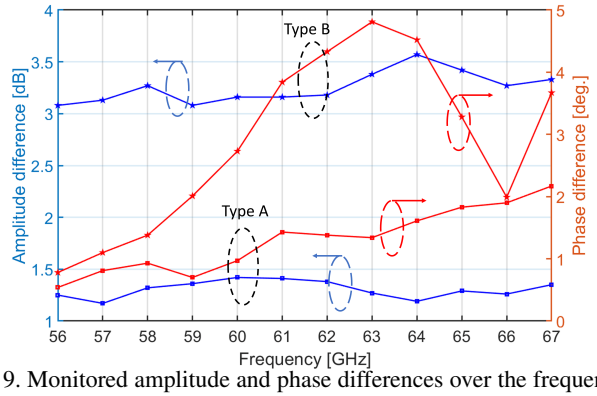

Fig. 9. Monitored amplitude and phase differences over the frequency for two types of H-plane unequal power dividers.

above the slot. To ease the fabrication process, the length of the larger brick is fixed at 2.4 mm. The smaller brick is with a length of 2.2 mm and 1.5 mm for type A and B power dividers. From the results, it can be seen for both types, the phase differences over the frequency between the two paths are within 5°. The amplitude variation of type A and type B is -1.3 ± 0.15 dB and -3.37 ± 0.3 dB, respectively. The amplitude and phase balances are worse than that of the E-planes power dividers. But from the previous study in [16], the performance is acceptable to achieve reasonably good radiation patterns within the operating range.

C. Feeding Network Unequal Power Divider

The power split ratio type C is achieved in the feeding network by a wideband unequal E-plane T-junction power divider. The structure is shown in Fig. 10 while the top layer is hidden to reveal the detailed view.

The design procedure is close to the conventional H-plane T-junction in [28], [29]. The structure is designed symmetrically with the input branch. Then a septum is placed inside one of the output branches to create a narrow gap. It is aligned with the left edge of the input waveguide. The power split ratio is adjusted by changing the length of the septum. A narrower gap introduces a larger power split ratio. The phase difference introduced by the offset septum is balanced using

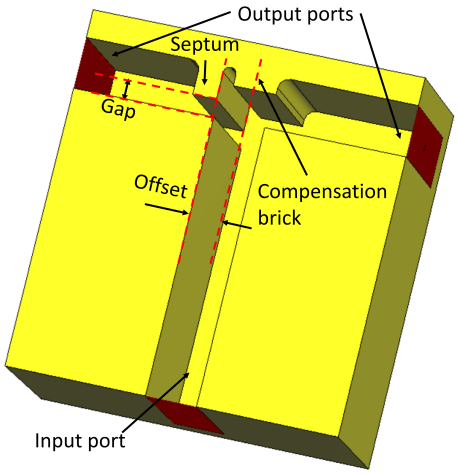

Fig. 10. The 3-D view of the E-plane T-junction unequal power divider.

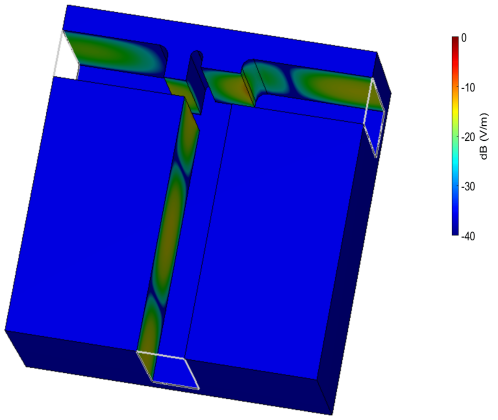

Fig. 11. The contour plot of the E-field distribution at the center frequency in T-junction.

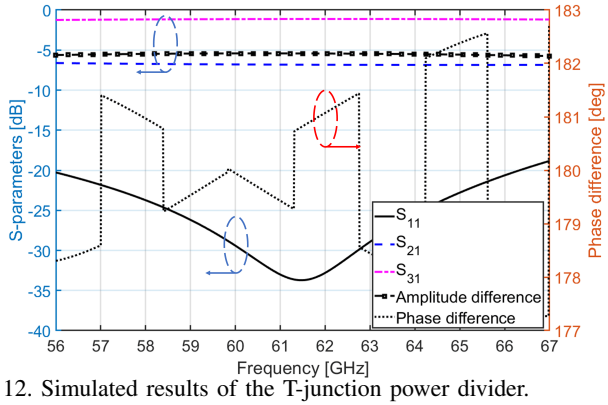

Fig. 12. Simulated results of the T-junction power divider.

a compensation brick by tuning its size and offset distance. The contour plot of the E-field distribution with a power split ratio of 5.61 dB at the center frequency is shown in Fig. 11. Apparently, less power is propagated into the left branch.

The optimized S-parameters are shown in Fig. 12. The amplitude difference is around −5.61 dB with a variation of ±0.1 dB over the frequency. The phase difference is within 180°±3°. In the operating range, the reflection coefficient below −19 dB is achieved. Compared to conventional H-plane T-junction, the amplitude and phase are more stable, and the structure is more compact in the proposed design. And the amplitude and phase variations over the frequency are more stable than the E-plane T-junction proposed in [16]. The corresponding parameters of the E-plane T-junction power dividers are shown in Table III.

V. Design of the Full Structure

A. One to four power dividers

The last stage of the feeding networks consists of two cascaded E-plane T-junctions with equal power split ratio and a transition section from the standard waveguide port (Wr-15). The combined structure is shown in Fig. 13. One additional layer with a standard waveguide port is hidden in the back. The structures of the feeding networks for the two polarization are the same. The transition sections are extended in two opposite directions to avoid interference as the cut view in Fig. 5. One

Table III. Optimized parameters of the E-plane T-junction power dividers.

	Length	Width
Input and output branches	3.5mm	1.2mm
Septum	0.79mm	0.56mm
Compensatoin brick	1mm	0.4mm
Offset distance	0.77mm	

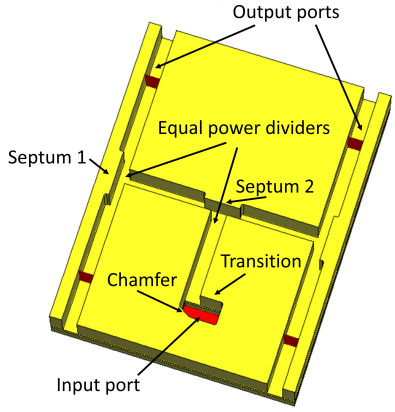

(a)

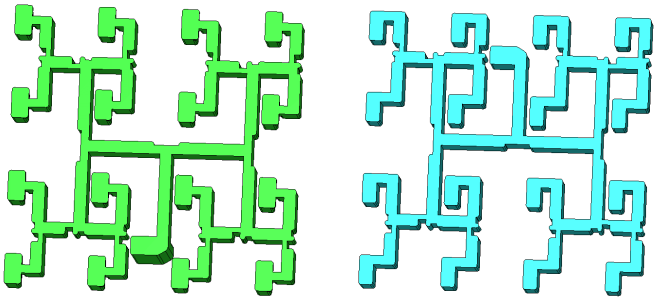

(b) (c)

Fig. 13. The 3-D view of (a) the combined structure of two-level T-junctions and a transition section from Wr-15, (b) the Vertically polarized feeding network, and (c) the Horizontally polarized feeding network.

septum for each level of T-junction is inserted for impedance matching. The simulated results of the combined structure are shown in Fig. 14. The reflection coefficient is below −18 dB from 57 to 66 GHz with a transmission loss within 0.34 dB. The output variations are within 0.2 dB. The corresponding parameters are listed in Table IV.

B. Simulation of the Whole Antenna

The design procedure of the antenna is as follows: First, the power-split ratio for the E- and H-plane subarray power dividers are adjusted to get the three types of the subarray, as shown in Fig. 5. In the second step, the subarrays are cascaded by two stages of the feeding network power dividers. Then, one-quarter of the antenna is obtained, which is symmetrical by two axes. Finally, the whole antenna is optimized by combining the quarter structures with the one to four power divider and the transition part. The optimization is towards better

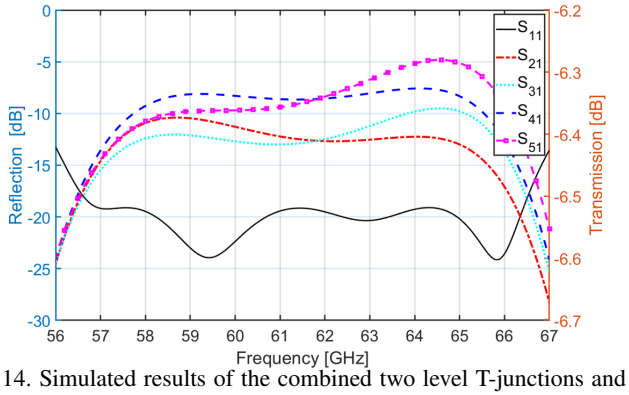

Fig. 14. Simulated results of the combined two level T-junctions and transition section.

Table IV. Optimized parameters of the combined two level T-junctions and transition section.

	Length	Width
T-junction Branches	3.5mm	1.25mm
Septum 1	3.7mm	0.36mm
Septum 2	3mm	0.44mm
Chamfer	1mm	31° (angle)
Transition section	3.2mm	1.88mm

impedance matching and in line with the target excitation tapering. An extension of 4 mm at each edge of the structure is added for positioning pins and screw holes. The overall size of the antenna is 40 mm × 40 mm with a thickness of 12.7 mm. All the corners in the design are changed to round with a radius of 0.5 mm to comply with the fabrication. The full antenna is optimized with open boundary (add space) conditions in CST.

The amplitude and phase distribution along the center element is monitored along the top surface of the antenna and plotted in Fig. 15. Only the E-plane of V-polarization is shown, as the amplitude tapering and the feeding network is symmetrical by two axes. The black dotted line in amplitude distribution is the theoretical distribution calculated in section II. It can be noticed that the amplitude of the center elements complies with the calculation very well. The amplitude distortion of far elements becomes large due to the influences from the extended edges. The phase difference among elements is within 15°. The simulated results can be considered stable compared with the former study in [16].

VI. Experimental Results

A test sample of the design is fabricated with the computerized numerical control (CNC) machine (DMG ecoMill 50). The assembled prototype and detailed structure of each layer is shown in Fig. 16. Eight screws around the edge of the sample are used to stack these layers up. Two sets of positioning pins are used to ensure the alignment of the layers. The extra adapter layer shown in Fig. 16(a) with two standard waveguide ports (Wr-15) is used to ease the connection with the frequency extender in the measurements. As shown in Fig. 16(b), layer one is the radiating layer with cross-shaped slots. H- and V-plane subarray power dividers are in layers two and three.

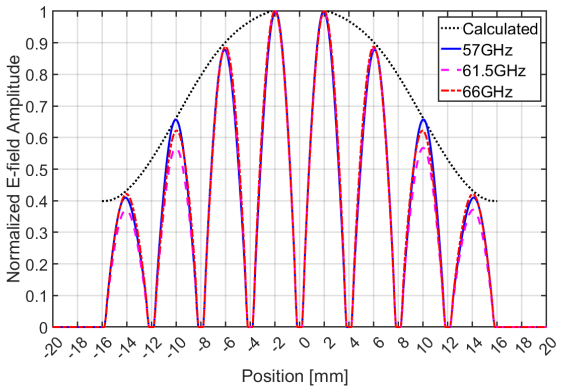

(a)

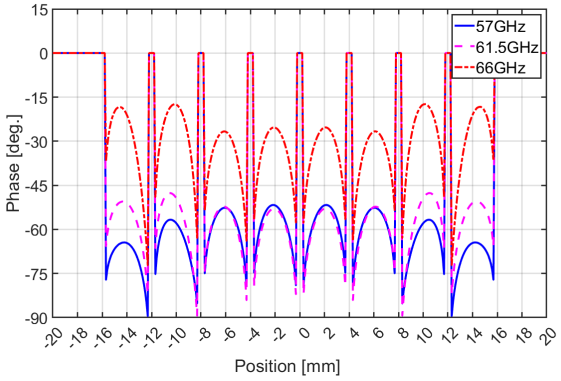

(b)

Fig. 15. Monitered (a) amplitude and (b) phase distribution along the center elements at different frequencies.

The feeding networks for the two polarizations are contained in layers four and five. The material used in the fabrication is brass, with close electrical characteristics to the simulation. The surface roughness is controlled within 0.0008 mm in the fabrication.

The prototype is measured in the anechoic chamber at Antennas, Propagation, and Millimeter-wave Systems laboratory at Aalborg University. The measured reflection coefficients and isolation are compared with the simulations in Fig. 17. In the simulation, a reflection coefficient smaller than −10 dB can be achieved in an overlapped frequency range from 56.4 to 66.4 GHz. The measured results distorted and shifted towards the high-frequency band due to fabrication accuracy and measurement deviation. However, the overlapped frequency range can still cover the entire V-band. A reasonably good isolation around 35 dB is achieved in the measurement.

The measured radiation patterns are shown in Fig. 18 and Fig. 19 for V-polarization and H-polarization, respectively. The dashed lines depicted are the class II sidelobe requirement from the ETSI frequency range 6 (47 - 66 GHz). It can be seen that for both polarizations, the measured patterns comply with the requirement, besides the grating lobes appearing at around ±90° at 66 GHz. Typically, an element spacing within one wavelength for a uniformed excited array can avoid the grating lobes. The grating lobe appears in the patterns because no grating lobe condition is reduced as amplitude tapering is applied. At 66 GHz, the corresponding wavelength is 88% in free space, which is closely the 89% wavelength

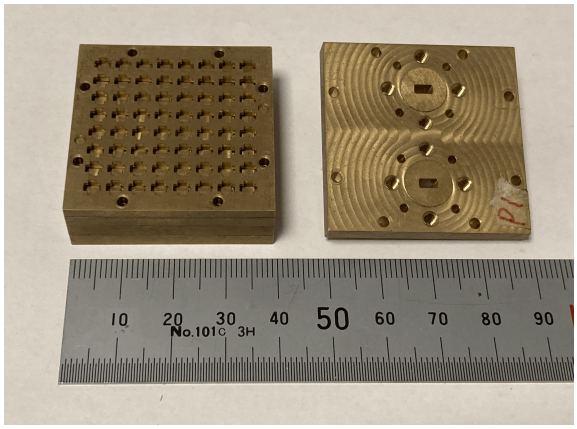

(a)

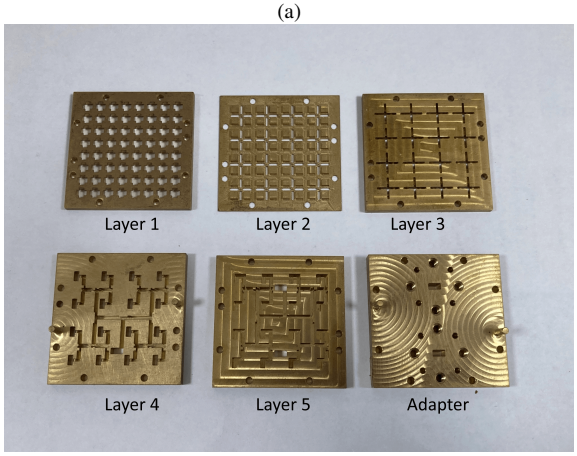

(b)

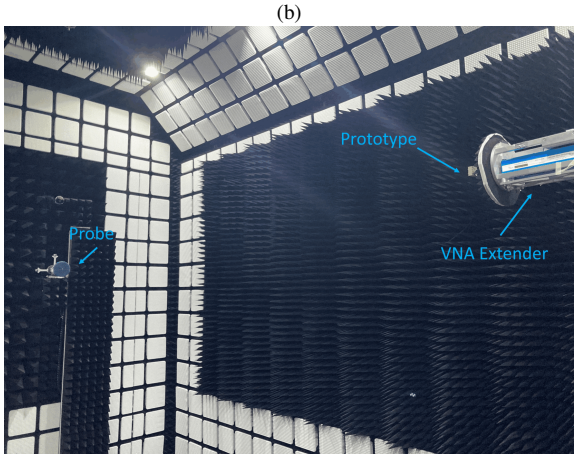

(c)

Fig. 16. Photographs of the fabricated antenna: (a) the assembled antenna and the adapter; (b) each of the layers; (c) measurement setup.

no grating lobe condition in [30]. The measured patterns are slightly distorted compared with the simulations due to the fabrication and assemble tolerance and some deviation in the measurement. Also, the instability of the amplitude distribution and phase unbalance can sometimes lead to pattern distortion. However, The measured patterns still agree with the simulations well in general. The depicted angle range is from -100° to 100°, as the back lobes can not be measured accurately due to the blockage of the frequency extender.

It can be observed that the maximum SLL in all patterns is below −22 dB. As the targeted first SLL is −25 dB in

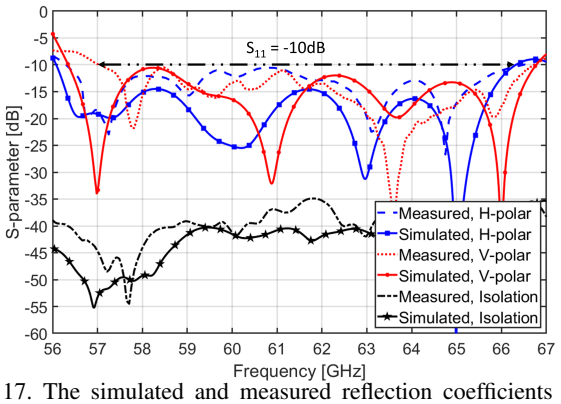

Fig. 17. The simulated and measured reflection coefficients of the prototype.

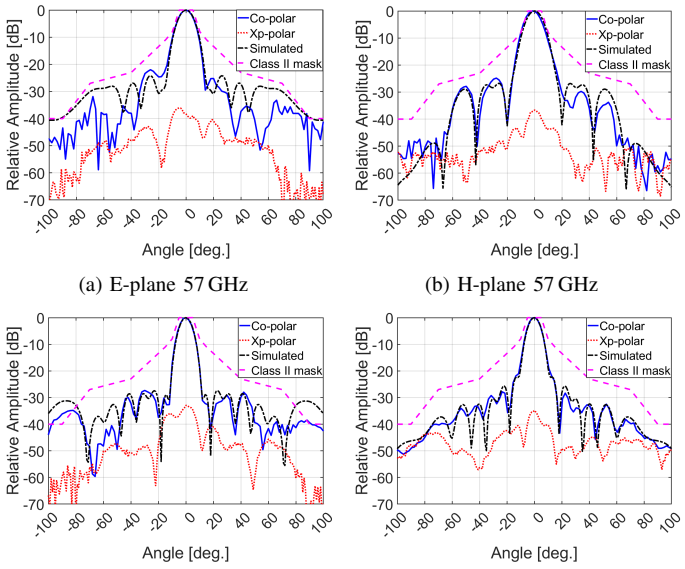

(a) E-plane 57 GHz (b) H-plane 57 GHz

(c) E-plane 66 GHz (d) H-plane 66 GHz

Fig. 18. Measured co-polarization (Co-polar) and cross-polarization (Xp-polar) radiation patterns of V-polarization at (a) E-plane 57 GHz, (b) H-plane 57 GHz, (c) E-plane 66 GHz, and (d) H-plane 66 GHz.

the theoretical calculation, the amplitude tapering and phase balance among elements is well controlled with the unequal power dividers. And no SLL rising from 30° to 50° from the boresight proves that each element's independent tapering excitation is effective. The cross-polarization levels are around 33 dB in all frequencies and polarizations.

The measured realized gains for both polarizations are compared with simulations in Fig. 20. The peak gain is 25.3 dBi and 25.4 dBi for V- and H- polarization, respectively. The gain fluctuations are mainly due to the fabrication and measurement tolerances. Also, the unstable amplitude tapering and phase unbalance variations over the frequency can also cause gain variations. As it is unable to measure the antenna efficiency in the chamber due to equipment limitations, the total efficiency of the prototype is estimated using the measured antenna gains and the simulated antenna directivities. In the whole V-band, an efficiency of around 60% can be achieved in both polarizations. And the aperture efficiencies are around 50%. The feeding network losses are evaluated with the measured reflection and estimated antenna total efficiencies.

Table V. Compared results between the proposed and other reported low SLL array antennas.

Works	Polarization	Aperture size, ($\lambda_0 \times \lambda_0$)	Gain (Min/Max), (dBi)	Technology	Center Frequency, (GHz)	BW (-10dB), (%)	Antenna Efficiency, (%)	Max SLL, (dB)
Ref. [22]	Single LP	12.16×12.16	25 / 29.5	H-plane HW	15.2	13.8	60	around -23
Ref. [23]	Single LP	11.73×11.73	28.8 / 29.9	IMGW	40	18.5	50 (η_e)	-23
Ref. [24]	Single LP	13.28×13.28	31.8 / 32.6	H-plane HW	73.5	9.8	72 (η_e)	-20 / -13.2
Ref. [25]	Dual CP	10.3×10.3	25.5 / 26	SIW PPLS	94	>1.1	57.5	-18.5
Ref. [26]	Dual LP	11.2×11.2	28 / 29.5	RGW	28	5.0 / 5.2	50	-18.5
This work	Dual LP	8.2×8.2	23.5 / 25.4	E-plane HW	15.2	8.4 - 11.4	60	-22

* The data in the table are calculated based on the −10 dB impedance bandwidth provided in the references.

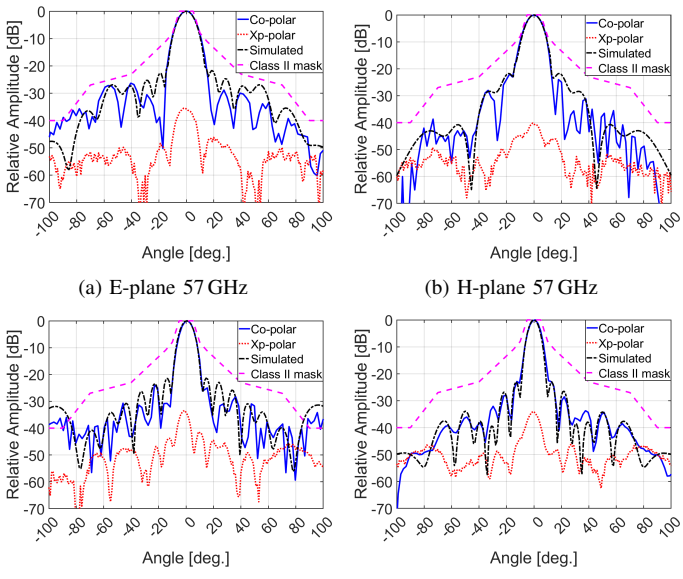

(a) E-plane 57 GHz (b) H-plane 57 GHz

(c) E-plane 66 GHz (d) H-plane 66 GHz

Fig. 19. Measured co-polarization (Co-polar) and cross-polarization (Xp-polar) radiation patterns of H-polarization at (a) E-plane 57 GHz, (b) H-plane 57 GHz, (c) E-plane 66 GHz, and (d) H-plane 66 GHz.

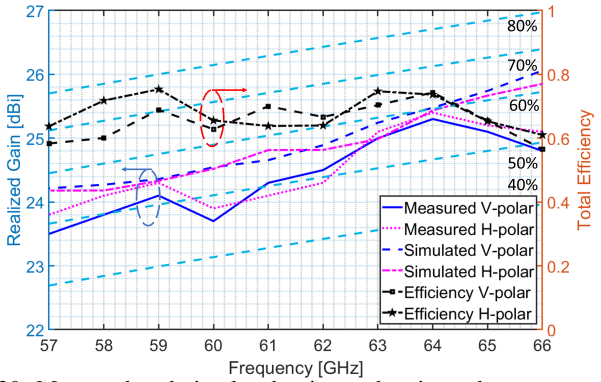

Fig. 20. Measured and simulated gains and estimated antenna total efficiencies of the prototype.

The obtained values are 1.66 dB and 1.53 dB for H- and V-polarization, respectively, which include the conductor losses, discontinuity losses, losses caused by fabrication errors, etc.

A comparison between the proposed structure and other reported low SLL array antennas is listed in Table V. In [22], [23], impressive first SLL levels are achieved. But the grating lobes that appear at 30° to 50° are even higher, which could still lead to interference issues. The high aperture efficiency in [24] is due to the unsuppressed H-plane SLL. Its maximum SLL is still around −13 dB. A common problem with single-polarization arrays is that they are difficult to be transformed into dual-polarization arrays by introducing another layer feeding network. The sidelobes rising problem also appeared in the referenced dual-polarized arrays, while it is not severe in [26]. However, they both suffer from narrow bandwidth. On the contrary, the proposed antenna has a wide overlapped impedance bandwidth with acceptable efficiency compared to the others. Furthermore, no apparent SLL rising from 30° to 50° be observed in all planes.

VII. Conclusion

In this paper, a dual-polarized low sidelobe slots array antenna is presented. Taylor distribution is applied in both polarizations. With the design of a compact 2×2 elements subarray and three types of compact unequal power dividers, the amplitude tapering of every radiating element can be adjusted independently. A prototype of 8×8 elements is fabricated and measured. An overlapped impedance bandwidth from 57 to 66.4 GHz is achieved, which covers the whole V-band. In the operating range, the measured radiation patterns comply with ETSI class II requirements in all azimuth planes with the maximum sidelobe level of −22 dB. The measured realized gain of both polarization is over 23.5 dBi with antenna efficiencies of round 60 %. The proposed structure shows the potential to substitute the conventional reflector antenna in a wireless communication system.

References

[1] M. Jaber, M. A. Imran, R. Tafazolli, and A. Tukmanov, "5G backhaul challenges and emerging research directions: A survey," *IEEE Access*, vol. 4, pp. 1743–1766, 2016.

[2] C. Dehos, J. L. González, A. De Domenico, D. Kténas, and L. Dussopt, "Millimeter-wave access and backhauling: the solution to the exponential data traffic increase in 5G mobile communications systems?," *IEEE Microw. Mag.*, vol. 52, no. 9, pp. 88–95, 2014.

[3] F. Foglia Manzillo, M. Śmierzchalski, L. Le Coq, M. Ettorre, J. Aurinsalo, K. T. Kautio, M. S. Lahti, A. E. I. Lamminen, J. Säily, and R. Sauleau, "A wide-angle scanning switched-beam antenna system in LTCC technology with high beam crossing levels for V-Band communications," *IEEE Trans. Antennas Propag.*, vol. 67, no. 1, pp. 541–553, 2019.

[4] W. Yang, K. Ma, K. S. Yeo, and W. M. Lim, "A compact high-performance patch antenna array for 60GHz applications," *IEEE Antenna Wireless Propag. Lett.*, vol. 15, pp. 313–316, 2016.

[5] Z. Chen, H. Liu, J. Yu, and X. Chen, "High gain, broadband and dual-polarized substrate integrated waveguide cavity-backed slot antenna array for 60GHz band," *IEEE Access*, vol. 6, pp. 31012–31022, 2018.

[6] Y. Li and K.-M. Luk, "Low-cost high-gain and broadband substrate-integrated-waveguide-fed patch antenna array for 60GHz band," *IEEE Trans. Antennas Propag.*, vol. 62, no. 11, pp. 5531–5538, 2014.

[7] J. Xu, Z. N. Chen, X. Qing, and W. Hong, "Bandwidth enhancement for a 60GHz substrate integrated waveguide fed cavity array antenna on LTCC," *IEEE Trans. Antennas Propag.*, vol. 59, no. 3, pp. 826–832, 2011.

[8] Y. Miura, J. Hirokawa, M. Ando, Y. Shibuya, and G. Yoshida, "Double layer full corporate feed hollow waveguide slot array antenna in the 60GHz band," *IEEE Trans. Antennas Propag.*, vol. 59, no. 8, pp. 2844–2851, 2011.

[9] M. Zhang, T. Yamamoto, J. Hirokawa, and M. Ando, "A wideband circularly polarized corporate-fed waveguide aperture array in the 60GHz band," *IEEE Antenna Wireless Propag. Lett.*, vol. 20, no. 9, pp. 1824–1828, 2021.

[10] A. Vosoogh and P.-S. Kildal, "Corporate-fed planar 60GHz slot array made of three unconnected metal layers using AMC pin surface for the gap waveguide," *IEEE Antenna Wireless Propag. Lett.*, vol. 15, pp. 1935–1938, 2016.

[11] A. Vosoogh, M. Sharifi Sorkherizi, V. Vassilev, A. U. Zaman, Z. S. He, J. Yang, A. A. Kishk, and H. Zirath, "Compact integrated full-duplex gap waveguide-based radio front end for Multi-Gbit/s point-to-point backhaul links at E-Band," *IEEE Trans. Microw. Theory Tech.*, vol. 67, no. 9, pp. 3783–3797, 2019.

[12] J. Liu, A. Vosoogh, A. U. Zaman, and J. Yang, "A slot array antenna with single-layered corporate-feed based on ridge gap waveguide in the 60GHz band," *IEEE Trans. Antennas Propag.*, vol. 67, no. 3, pp. 1650–1658, 2019.

[13] Y. Li, L. Ge, J. Wang, S. Da, D. Cao, J. Wang, and Y. Liu, "3-D printed high-gain wideband waveguide fed horn antenna arrays for millimeter-wave applications," *IEEE Trans. Antennas Propag.*, vol. 67, no. 5, pp. 2868–2877, 2019.

[14] Y. Li, L. Ge, J. Wang, B. Ai, M. Chen, Z. Zhang, and Z. Li, "A *Ka*-band 3-D-Printed wideband stepped waveguide-fed magnetoelectric dipole antenna array," *IEEE Trans. Antennas Propag.*, vol. 68, no. 4, pp. 2724–2735, 2020.

[15] Z. Shi-Gang, H. Guan-Long, P. Zhao-hang, and L.-J. Ying, "A wideband full-corporate-feed waveguide slot planar array," *IEEE Trans. Antennas Propag.*, vol. 64, no. 5, pp. 1974–1978, 2016.

[16] P. Liu, G. F. Pedersen, and S. Zhang, "Wideband low-sidelobe slot array antenna with compact tapering feeding network for E-Band wireless communications," *IEEE Trans. Antennas Propag.*, vol. 70, no. 4, pp. 2676–2685, 2022.

[17] "Fixed radio systems characteristics requirements, standard etsi en 302 217-4-2 v1.5.1 (2010-01),European Telecommunications Standards, 2010. [online]. available: http://www.etsi.org/index.php,"

[18] T. Potelon, M. Ettorre, L. Le Coq, T. Bateman, J. Francey, D. Lelaidier, E. Seguenot, F. Devillers, and R. Sauleau, "A low-profile broadband 32-slot continuous transverse stub array for backhaul applications in *E*-Band," *IEEE Trans. Antennas Propag.*, vol. 65, no. 12, pp. 6307–6316, 2017.

[19] T. Tomura, Y. Miura, M. Zhang, J. Hirokawa, and M. Ando, "A 45° linearly polarized hollow-waveguide corporate-feed slot array antenna in the 60GHz band," *IEEE Trans. Antennas Propag.*, vol. 60, no. 8, pp. 3640–3646, 2012.

[20] A. Vosoogh, P.-S. Kildal, and V. Vassilev, "Wideband and high-gain corporate-fed gap waveguide slot array antenna with ETSI Class II radiation pattern in *V*-Band," *IEEE Trans. Antennas Propag.*, vol. 65, no. 4, pp. 1823–1831, 2017.

[21] C. A. Balanisn, "Antenna theory: Analysis and design," in *3rd ed. Hoboken, NJ, USA: Wiley*, p. 406–408, 2005.

[22] G.-L. Huang, S.-G. Zhou, T.-H. Chio, H.-T. Hui, and T.-S. Yeo, "A low profile and low sidelobe wideband slot antenna array feb by an amplitude-tapering waveguide feed network," *IEEE Trans. Antennas Propag.*, vol. 63, no. 1, pp. 419–423, 2015.

[23] J. Liu, F. Yang, K. Fan, and C. Jin, "Unequal power divider based on inverted microstrip gap waveguide and its application for low sidelobe slot array antenna at 39GHz," *IEEE Trans. Antennas Propag.*, vol. 69, no. 12, pp. 8415–8425, 2021.

[24] H. Arakawa, H. Irie, T. Tomura, and J. Hirokawa, "Suppression of e-plane sidelobes using a double slit layer in a corporate-feed waveguide slot array antenna consisting of 2×2 -element radiating units," *IEEE Trans. Antennas Propag.*, vol. 67, no. 6, pp. 3743–3751, 2019.

[25] Y. J. Cheng, J. Wang, and X. L. Liu, "94GHz substrate integrated waveguide dual-circular-polarization shared-aperture parallel-plate long-slot array antenna with low sidelobe level," *IEEE Trans. Antennas Propag.*, vol. 65, no. 11, pp. 5855–5861, 2017.

[26] J. Ran, C. Jin, P. Zhang, W. Wang, and Y. Wu, "High-gain and low-loss dual-polarized antenna array with reduced sidelobe level based on gap waveguide at 28GHz," *IEEE Antenna Wireless Propag. Lett.*, vol. 21, no. 5, pp. 1022–1026, 2022.

[27] S.-G. Zhou, Z.-H. Peng, G.-L. Huang, J.-Y. Li, and C.-Y.-D. Sim, "Design of wideband and dual polarized cavity antenna planar array," *IEEE Trans. Antennas Propag.*, vol. 64, no. 10, pp. 4565–4569, 2016.

[28] G.-L. Huang, S.-G. Zhou, T.-H. Chio, and T.-S. Yeo, "Design of a symmetric rectangular waveguide T-junction with in-phase and unequal power split characteristics," in *2013 IEEE Antennas and Propagation Society International Symposium (APSURSI)*, pp. 2119–2120, 2013.

[29] S. Christopher, V. Abid Hussain, M. Easwaran, and V. Dabade, "Design aspects of compact high power multiport unequal power dividers," in *Proceedings of International Symposium on Phased Array Systems and Technology*, pp. 63–67, 1996.

[30] P.-S. Kildal, *Foundations of Antenna Engineering: A Unified Approach for Line-of-Sight and Multipath*. Artech, 2015.

Peiye Liu received the M.S. degree in wireless and photonics engineering from Chalmers University of Technology, Gothenburg, Sweden, in 2016. After his M.S. studies, he joined Guangdong Shenglu Telecommunication Technology Co., Ltd, Foshan, China. He is now pursuing a Ph.D. degree in the Antennas, Propagation and Millimeter-Wave Systems Section, Department of Electronic Systems at Aalborg University, Aalborg, Denmark. His research interests include planner array antennas, mm-wave mobile antenna design, and interactions between users and mobile antennas.

Gert Frølund Pedersen was born in 1965. He received the B.Sc. and E.E. (Hons.) degrees in electrical engineering from the College of Technology in Dublin, Dublin Institute of Technology, Dublin, Ireland, in 1991, and the M.Sc.E.E. and Ph.D. degrees from Aalborg University, Aalborg, Denmark, in 1993 and 2003, respectively. Since 1993, he has been with Aalborg University, where he is a Full Professor heading the Antenna, Propagation, and Networking LAB with 36 researchers. He is also the Head of the Doctoral School on wireless communication with some 100 Ph.D. students enrolled. His research interests include radio communication for mobile terminals, especially small antennas, diversity systems, propagation, and biological effects. He has published more than 175 peer-reviewed papers and holds 28 patents. He has also worked as a Consultant for the development of more than 100 antennas for mobile terminals, including the first internal antenna for mobile phones in 1994 with the lowest SAR, the first internal triple-band antenna in 1998 with low SAR and high TRP and TIS, and lately various multiantenna systems rated as the most efficient on the market. He has worked most of the time with joint university and industry projects and has received more than 12 M$ in direct research funding. He is currently the Project Leader of the SAFE project with a total budget of 8 M$ investigating tunable front end, including tunable antennas for future multi-band mobile phones. He has been one of the pioneers in establishing over-the-air measurement systems. The measurement technique is now well-established for mobile terminals with single antennas. He was chairing the various COST groups (swg2.2 of COST 259, 273, 2100, and now ICT1004) with liaison to 3GPP for an over-the-air test of MIMO terminals. He is currently involved in MIMO OTA measurement.

Wonbin Hong received the B.S. degree in electrical engineering from Purdue University, West Lafayette, in 2004 and master's and Ph.D. degrees in electrical engineering from the University of Michigan at Ann Arbor in 2005 and 2009, respectively.

From 2009 to 2016, he was with Samsung Electronics as a Principal and a Senior Engineer, participating and leading extensive research and development tasks for upcoming wireless applications, including MIMO, wireless power transfer, and millimeter-wave wireless solutions. As of February 2016, he is with the Department of Electrical Engineering, Pohang University of Science and Technology (POSTECH) as an Associate Professor. He currently holds the Mueunjae Chaired Professorship. He has well over a decade of extensive research and development experience with primary interests in future wireless communication antennas and R.F. circuits, mesoscale and nanoscale transparent electronics, IoT/wearable devices based on advanced electromagnetics, and 3-D packaging. He is one of the first researchers to pioneer the concept and design of millimeter-wave antennas and R.F. front-ends in the field of consumer electronics, including mobile terminals and access points for the much anticipated ultrafast broadband wireless solutions, such as 5G and 6G. He has authored and co-authored more than 150 peer-reviewed journals, conference papers, and two book chapters, and is the inventor of more than 50 granted and 180 pending patents. He has been involved in more than 50 government and industry research projects. Currently, he serves as a technical consultant to numerous multinational tech firms, such as Samsung Electronics, Hyundai Motors, L.G. Electronics, SK Telecom, Sumitomo Chemical, Corning, LG Uplus, and several other confidential leaders in industry and government agencies.

His students have received recognition, including the Second Place Best Student Paper Award in the 2021 IEEE AP-S Symposium on Antennas and Propagation, the First Place Best Student Paper Award in the 2020 IEEE AP-S Symposium on Antennas and Propagation, the Best Student Paper Award IEEE European Conference on Antennas and Propagation 2020, the 2018 Outstanding Master's Student, Electrical Engineering Department of POSTECH, the Silver Medal in the 14th Samsung Electro-Mechanics Best Paper Award 2018, the First Prize Best Student Paper Award in 2018 IEEE International Symposium on Antennas and Propagation, and the Best Paper Award in 2017 ISMOT. He has served as an invited lecturer and speaker in over 100 international research symposiums, government and industry sessions held around the world. He is currently serving as an associate editor for the IEEE Transaction on Antennas and Propagation and IEEE Antennas and Propagation Magazine. He recently served as the guest editor of the IEEE Transaction on Antennas and Propagation special issue on "Low-Cost Beam Scanning Antenna" and the guest editor of Frontiers in Communication and Networks special issue on "mmWave Antennas and Testbeds." He has served as the lead guest editor for the IEEE Antennas and Wireless Propagation Letter special cluster on "Antenna-in-Package, Antenna-on-Chip, Antenna-IC Interface: Joint Design and Co-Integration" and also served as the guest editor for the IEEE Transaction on Antennas and Propagation special issue on "Antennas and Propagation Aspects of 5G Communications."

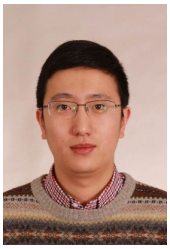

Shuai Zhang (SM'18) received the B.E. degree from the University of Electronic Science and Technology of China, Chengdu, China, in 2007 and the Ph.D. degree in electromagnetic engineering from the Royal Institute of Technology (KTH), Stockholm, Sweden, in 2013. In 2014, he joined Aalborg University, Denmark, where he is currently the head of the antenna research group with over 12 staff. He has also been admitted to a promotion program to a Professor at Aalborg University since 2022. In 2010 and 2011, he was a Visiting Researcher at Lund University, Sweden, and Sony Mobile Communications AB, Sweden, respectively. He was also an external antenna specialist at Bang & Olufsen, Denmark, from 2016-2017. He has supervised/co-supervised 7 Postdocs and 18 PhD students. He has co-authored over 115 articles in well-reputed international journals and over 16 U.S. or W.O. patents. His citations in Scopus are over 4000, with an H index of 32. His current research interests include: millimeter-wave antennas for cellular communications, bio-electromagnetics, metasurfaces, CubeSat antennas, Massive MIMO antennas, wireless sensors, and RFID antennas.

He is the Associate Editor for IEEE Antennas and Wireless Propagation Letters; Sensors; and IET Microwaves, Antennas and Propagation. He is also a reviewer for all the top IEEE and IET journals in antenna areas, where he won the prize of "Top Reviewers in IEEE Transactions on Antennas and Propagation 2019-2020 and 2020-2021". He is the General Co-Chair for iWAT2023 at Aalborg, Denmark, the Super Reviewer (previously known as Super TPC or Vice Chair) for IEEE APS 2020 and 2021, and the TPC for several top IEEE conferences. He is the recipient of "IEEE Antennas and Propagation Society Young Professional Ambassador" in 2022, where he gives presentations for different IEEE Chapters on Antennas for Cellular Communications. He has also been intensively invited to international conferences and industry to give keynote/plenary speeches and presentations. From 2019-2023, He is the Management Committee for EU COST Action CA18223 of SyMat, which mainly focuses on highly symmetrical periodic structures or metamaterials.